
Understanding DDPM Latent Codes Through Optimal Transport

Valentin Khruikov^{1,2} Ivan Oseledets^{2,3}

Abstract

Diffusion models have recently outperformed alternative approaches to model the distribution of natural images, such as GANs. Such diffusion models allow for deterministic sampling via the probability flow ODE, giving rise to a latent space and an encoder map. While having important practical applications, such as estimation of the likelihood, the theoretical properties of this map are not yet fully understood. In the present work, we partially address this question for the popular case of the VP SDE (DDPM) approach. We show that, perhaps surprisingly, the DDPM encoder map coincides with the optimal transport map for common distributions; we support this claim theoretically and by extensive numerical experiments.

1. Introduction

Denosing diffusion probabilistic models (DDPMs) (Sohl-Dickstein et al., 2015; Ho et al., 2020) have recently outperformed alternative approaches to model the distribution of natural images both in the realism of individual samples and their diversity (Dhariwal & Nichol, 2021). These advantages of diffusion models are successfully exploited in applications, such as colorization (Song et al., 2021b), inpainting (Song et al., 2021b), super-resolution (Saharia et al., 2021; Li et al., 2022), and semantic editing (Meng et al., 2022), where DDPM often achieve more impressive results compared to GANs.

One crucial feature of diffusion models is the existence of a deterministic invertible mapping from the data distribution to the limiting distribution of the diffusion process, commonly being a standard normal distribution. This approach termed denosing diffusion implicit model (DDIM) (Song et al., 2021a), or the probability flow ODE in the continuous model (Song et al., 2021b), allows to invert real images easily, perform data manipulations, obtain a uniquely iden-

tifiable encoding, as well as to compute exact likelihoods. Despite these appealing features, not much is known about the actual mathematical properties of the encoder map and corresponding latent codes, which is the question we address in this work. Concretely, in this paper, we propose and validate the following hypothesis: for the DDPM diffusion process, based on the Variance Preserving (VP) SDE (Song et al., 2021b), this encoder map is the *Monge optimal transport map* between the data distribution and the standard normal distribution. We provide both theoretical and extensive empirical evidence on controlled synthetic examples and real datasets, showing that these two maps are equal, with the proof given in the case of multivariate normal distributions. Our findings suggest a complete description of the encoder map and an intuitive approach to understanding the ‘structure’ of a latent code for DDPMs trained on visual data. In this case, the pixel-based Euclidean distance corresponds to high-level texture and color-based similarity, directly observed on real DDPMs. To summarize, the contributions of our paper are:

1. We state the hypothesis that the DDPM encoder map is the Monge optimal transport map and verify it theoretically for the case of multivariate normal distributions.
2. We investigate it numerically on a large class of synthetic distributions and show that the equality holds up to negligible errors.
3. We provide additional empirical evidence supporting our hypothesis on real image datasets.

2. Reminder on diffusion models

We start by recalling various concepts from the theory of diffusion models and stochastic differential equations (SDEs).

2.1. Denosing diffusion probabilistic models

Denosing diffusion probabilistic models (DDPMs) is a class of generative models recently shown to obtain excellent performance on the task of image synthesis (Dhariwal & Nichol, 2021; Ho et al., 2020; Song et al., 2021b). We start with a forward (non-parametric) diffusion which gradually adds noise to data, transforming it to a Gaussian distribution.

*Equal contribution ¹Yandex, Moscow, Russia ²Skoltech, Moscow, Russia ³AIRI, Moscow, Russia. Correspondence to: Valentin Khruikov <khruikov.v@gmail.com>.

Formally, we specify the transitions probabilities as

$$q(x_t|x_{t-1}) := \mathcal{N}(x_t; \sqrt{1 - \beta_t}x_{t-1}, \beta_t I), \quad (1)$$

for some fixed variance schedule β_1, \dots, β_t . Importantly, a noisy sample x_t can be obtained directly from the clean sample x_0 as $x_t = \sqrt{\bar{\alpha}_t}x_0 + \sqrt{1 - \bar{\alpha}_t}\mathbf{z}$, with $\mathbf{z} \sim \mathcal{N}(0, I)$ and $\alpha_t := 1 - \beta_t$, $\bar{\alpha}_t := \prod_{s=1}^t \alpha_s$. The generative model then learns to reverse this process and thus gradually produce realistic samples from noise. Specifically, DDPM learns parameterized Gaussian transitions:

$$p_\theta(x_{t-1}|x_t) := \mathcal{N}(x_t; a_\theta(x_t, t), \sigma_t). \quad (2)$$

In practice, rather than predicting the mean of the distribution in Equation (2), the noise predictor network $\epsilon_\theta(x_t, t)$ predicts the noise component from the sample x_t and the step t ; the mean is then a linear combination of this noise component and x_t . The covariances σ_t can be either fixed or learned as well; the latter was shown to improve the quality of models (Nichol & Dhariwal, 2021). Interestingly, the noise predictor $\epsilon_\theta(x_t, t)$ is tightly related to the *score function* (Stein, 1972; Liu et al., 2016; Gorham, 2017) of the intermediate distributions; specifically by defining $s_\theta(x_t, t)$ as

$$s_\theta(x_t, t) = \frac{\epsilon_\theta(x_t, t)}{\sqrt{1 - \bar{\alpha}_t}} \quad (3)$$

we obtain that $s_{\theta^*}(x_t, t) \approx \nabla_x \log p_t(x_t)$, with $p_t(x_t)$ being the density of the target distribution after t steps of the diffusion process and θ^* are the parameters at convergence.

Stochastic and deterministic sampling. Given the DDPM model, the generative process is expressed as

$$x_{t-1} = \frac{1}{\sqrt{\alpha_t}} \left(x_t - \frac{1 - \alpha_t}{\sqrt{1 - \bar{\alpha}_t}} \epsilon_\theta(x_t, t) \right) + \sigma_t \mathbf{z},$$

with the initial sample $x_T \sim \mathcal{N}(0, I)$ and $\mathbf{z} \sim \mathcal{N}(0, I)$. The sampling procedure is stochastic, and no single ‘latent space’ exists. The authors of Song et al. (2021a) proposed a deterministic approach to produce samples from the target distribution, termed DDIM (denoising diffusion implicit model). Importantly, this approach does not require retraining DDPM and only changes the sampling algorithm; the obtained marginal probability distributions p_t are equal to those produced by the stochastic sampling. It takes the following form:

$$x_{t-1} = \sqrt{\bar{\alpha}_{t-1}} \left(\frac{x_t - \sqrt{1 - \bar{\alpha}_t} \epsilon_\theta(x_t, t)}{\sqrt{\bar{\alpha}_t}} \right) + \sqrt{1 - \bar{\alpha}_{t-1}} \cdot \epsilon_\theta(x_t, t). \quad (4)$$

By utilizing DDIM, we obtain a concept of a latent space and encoder for diffusion models, since the only input to the generative model now is $x_T \sim \mathcal{N}(0, I)$ for sufficiently large T . In the next section, we will see how it is defined in the continuous setup.

2.2. SDE view on Diffusion Models

The authors of Meng et al. (2022) proposed to view diffusion models as a discretization of certain stochastic differential equations. SDEs generalize standard ordinary differential equations (ODEs) by injecting random noise in dynamics. Specifically, the diffusion process specified by Equation (1) is a discretization of the following SDE:

$$dx = -\frac{1}{2}\beta(t)xdt + \sqrt{\beta(t)}dw. \quad (5)$$

where dx is an increment of x over the infinitesimal time step dt . Here, w represents a Brownian motion process, so dw can be intuitively understood as an infinitesimal Gaussian noise. Similar to DDPMs, an initial distribution with density p_0 evolves into a standard normal distribution under this SDE. Various DDPM algorithms can be seen as discretizations of SDE-based algorithms. The continuous analogue of DDIM sampling (4) is given by the following (deterministic) ODE (Song et al., 2021b):

$$dx = -\frac{\beta(t)}{2} [x + \nabla_x \log p_t(x)] dt, \quad (6)$$

with $p_t(x)$ being the density at time t ; the score function $\nabla_x \log p_t(x)$ is similarly approximated via a neural network during training. The limiting distribution then serves as the *latent space*; sampling is performed by reversing this ODE. Moreover, the DDIM sampling can be seen as a numerical integration scheme for this ODE (Salimans & Ho, 2022).

The well-developed theory of SDEs provides us with a rigorous mathematical apparatus allowing us to study the properties of diffusion models at hand. We will utilize the following well-known equation termed the forward Kolmogorov, or Fokker-Planck equation (Risken, 1996). This equation determines how a density p_0 evolves under a (general) SDE. For (5) it takes the following form:

$$\frac{\partial p_t}{\partial t} = \frac{\beta(t)}{2} [\nabla_x \cdot (xp_t) + \nabla_x^2 p_t]. \quad (7)$$

Note, that $\beta(t)$ can be removed from (7) by change of variables $dt := \frac{\beta(t)}{2} dt$, resulting in the PDE of the form

$$\frac{\partial p_t}{\partial t} = \nabla_x \cdot (xp_t) + \nabla_x^2 p_t. \quad (8)$$

Without loss of generality, we will work with this simplified equation since the specific form of $\beta(t)$ does not affect the results. In this case, the probability flow ODE takes the following form:

$$dx = -[x + \nabla_x \log p_t(x)] dt. \quad (9)$$

Encoder map. As mentioned above, by considering the probability flow ODE (6), we can obtain latent codes for

samples from the original distribution. For a given distribution μ_0 and a timestep t , let us denote the flow generated by this vector field as $E_{\mu_0}(t, \cdot)$. I.e., a point $x \sim \mu_0$ is mapped to $E_{\mu_0}(t, x)$ when transported along the vector field for a time t . The ‘final’ encoding map is obtained when $t \rightarrow \infty$, i.e.

$$E_{\mu_0}(x) := \lim_{t \rightarrow \infty} E_{\mu_0}(t, x).$$

Note that E_{μ_0} implicitly depends on all the intermediate densities μ_t obtained from the diffusion process (or the Fokker-Planck equation).

3. DDPM Encoder and Optimal Transport

By construction and properties of the phase flow, the map E_{μ} transforms the original distribution μ_0 into the standard normal distribution $\pi := \mu_{\infty} \sim \mathcal{N}(0, I)$. Our further analysis investigates a perhaps surprising hypothesis that this map is the *optimal transport* map. How to arrive at this idea? A priori, it seems nontrivial that the theory of optimal transportation is related to the Fokker-Planck equation and diffusion processes. Some intuition may be obtained from the Otto calculus (Otto, 1996; 2001; Villani, 2009). It presents an alternative view on the solutions of the Fokker-Planck-type PDEs and diffusion equations in the following manner. It can be shown that the trajectory $\{\mu_t\}_{t=0}^{\infty}$, obtained by solving the Fokker-Planck equation (or an equivalent diffusion SDE), is, in fact, the *gradient flow* of a certain functional in the *Wasserstein space* of probability measures. Moreover, locally, optimal transport maps between two ‘consecutive’ densities (i.e., separated by an infinitesimal time interval) along this trajectory are given precisely by the flow of the ODE (6). Thus, this trajectory is generally a sequence of infinitesimal optimal transports, which may not result in the ‘global’ optimal transport map. However, our experiments suggested that in the case when the target density is $\mathcal{N}(0, I)$ as in DDPMs, this map *is* the optimal transport map. We start with a toy example and then proceed to more general cases.

3.1. Toy example

One of the few cases when both optimal transport and diffusion equations can be solved explicitly is the case of multivariate Gaussian distributions. For simplicity, in this example, we consider $\mu_0 \sim \mathcal{N}(a, I)$ with $a \in \mathbb{R}^n$ and $I \in \mathbb{R}^{n \times n}$ being the identity matrix. Rather than utilizing Equation (8) to obtain intermediate density values, we can do it directly from the transition formulas for SDE (5) found in Song et al. (2021b); Särkkä & Solin (2019); the corresponding probabilities then take the form:

$$\mu_t \sim \mathcal{N}(ae^{-t}, I). \quad (10)$$

The probability flow ODE takes the form

$$\frac{dx}{dt} = -ae^{-t}. \quad (11)$$

Solving this ODE amounts to simply integrating the function in the right-hand side, and in the limit $t \rightarrow \infty$ we obtain $E_{\mu_0}(x) = x - a$. Note that this is exactly the optimal transport map between μ_0 and $\mathcal{N}(0, I)$.

3.2. Reminder on optimal transport

We now briefly recall the main definitions of the optimal transport theory. For a thorough review of optimal transport, we refer the reader to classical texts such as Thorpe (2018); Villani (2009); Ambrosio et al. (2005).

Kantorovich and Monge formulation. Suppose we have two random variables with densities μ and ν supported on spaces X and Y respectively (in our work, we only consider distributions in Euclidean spaces). We consider the *optimal transport problem* between μ and ν . There are several possible formulations of this task, namely Kantorovich formulation and Monge formulation. Under quite general assumptions, these two formulations are equivalent. We will start from the Kantorovich formulation. In this formulation, we consider densities $\gamma \in \mathcal{P}(X \times Y)$ such that their marginal densities are μ and ν respectively. Such set is denoted by $\Pi(\mu, \nu)$ and its elements are termed *transport plans*. The Kantorovich formulation of the optimal transport problem is finding the *optimal* transport plan:

$$\int c(x, y)\gamma(x, y)dxdy \rightarrow \min_{\gamma \in \Pi(\mu, \nu)}, \quad (12)$$

where $c(x, y)$ is a cost function. Under quite general assumptions on μ, ν , there exists a unique solution to the Kantorovich problem. Rather than working with transport plans, it is more convenient to work with transport maps, which provide means to actually move one distribution to another. In this formulation (termed the Monge formulation), our goal is finding a *transport map* $S : X \rightarrow Y$ such that

$$\int c(x, S(x))\mu(x)dx \rightarrow \inf_S, \quad (13)$$

over all μ -measurable transport maps S such that $\nu = S_{\#}\mu$. Here, $S_{\#}\mu$ is the push-forward measure, i.e., $(S_{\#}\mu)(A) = \mu(S^{-1}(A))$ for all measurable sets A . For smooth and bijective maps S this condition can be also written as $\mu(x) = \nu(S(x))|\det \nabla S|$, where ∇S is the Jacobian matrix of S . Due to the high nonlinearity of this equation, solving it directly is a nontrivial task.

Importantly, for *non-atomic* measures, these two definitions are equivalent (Villani, 2009). Given an optimal transport map, it can be straightforwardly converted to the optimal

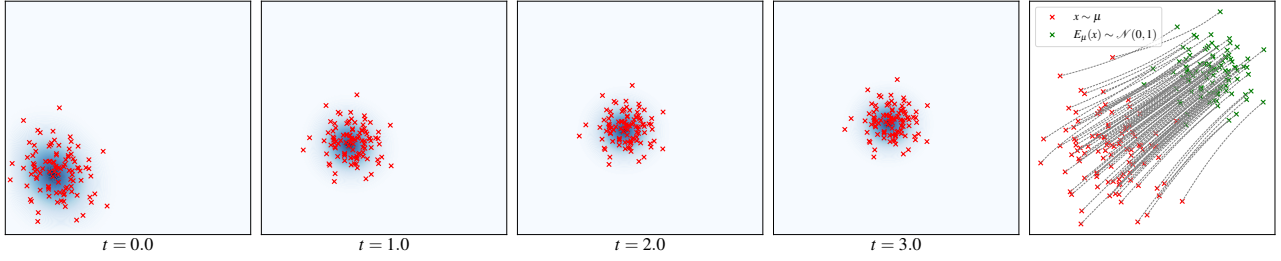


Figure 1: A toy example of our approach on a $2d$ multivariate normal distribution μ . The first four plots visualize the diffusion process. The fifth plot demonstrates the trajectories of the probability flow ODE. In this case, the optimal transport map is known analytically and exactly coincides with the mapping E_μ , introduced in Section 2. Note that the trajectories of the probability flow ODE are not straight lines even in this simple case.

transport plan. Such a plan is deterministic, as we know precisely where to move each point. In this work, we consider the quadratic cost function, i.e.,

$$c(x, y) = \|x - y\|^2,$$

as commonly done in the study of diffusion equations and gradient flows in Wasserstein spaces (Villani, 2009). In this case, the distance between distributions is denoted as $W_2(\cdot, \cdot)$ and is given by the square root of the optimal transport cost (12).

Benamou-Brenier formulation. It will be instructive to consider another formulation of the optimal transport, originating in spirit from the fluid dynamics (Benamou & Brenier, 2000; Villani, 2003). Assume that at $t = 0$ we are given a set of ‘particles’ from the density ρ_0 which move in such a way that at $t = 1$ their state is described by the density ρ_1 . Moreover, these particles move in such that they perform the least amount of work. Formally, they minimize the following *action*:

$$A = \int_0^1 \left(\sum_x |\dot{x}(t)|^2 \right) dt,$$

with x varying in the set of particles. In the continuous limit, we obtain the following formulation (with v_t being the velocity field):

$$\inf_{\rho, v} \left\{ \int_0^1 \int \rho_t(x) |v_t(x)|^2 dx dt; \quad \frac{\partial \rho_t}{\partial t} + \nabla \cdot (\rho_t v_t) = 0 \right\} \quad (14)$$

where the infimum is taken over all time-dependent probability densities $\{\rho_t\}_{t=0}^1$ which agree with ρ_0 and ρ_1 at respective times $t = 0$ and $t = 1$, and overall time-dependent velocity fields $\{v_t\}_{t=0}^1$ which convect ρ_t , as expressed by the continuity equation in the right-hand side of Equation (14).

It can be shown that the infimum in Equation (14) is given by $W_2(\rho_0, \rho_1)^2$. Moreover, given an optimal transport map

we can easily construct the corresponding admissible trajectory for the Benamou-Brenier formulation. If S is the optimal Monge map, we set $S(t, x) = (1-t)x + tS(x)$ and $v_t(x) = \left(\frac{d}{dt}S(t, x)\right) \circ S(t, x)^{-1}$. Then, $\rho_t = S(t, \cdot)_\#(\rho_0)$. Importantly, trajectories generated by this vector field are *straight lines*, which does not hold for the probability flow ODE (see, e.g., Figure 1). There is no contradiction here: we do not claim that the probability flow ODE is the solution of the Benamou-Brenier problem, but only that the flow map induced by this ODE (in the limit $t \rightarrow \infty$) solves the Monge problem. So, in general, the vector field solving (14) and the vector field of the probability flow ODE will be different.

3.3. Multivariate normal distribution case

We start by showing theoretically that for an arbitrary multivariate normal distributions, the DDPM encoder map coincides with the optimal transport map. This map is known analytically for normal distributions in the case of the quadratic cost function (Givens & Shortt, 1984).

Theorem 3.1. *Let $\mu_0 \sim \mathcal{N}(a(0), \Sigma(0))$ be a multivariate normal distribution. Then E_{μ_0} is the Monge optimal transport map between μ_0 and $\mathcal{N}(0, I)$, i.e.,*

$$E_{\mu_0}(x) = \Sigma(0)^{-1/2}(x - a(0)).$$

Proof. The proof is based on the fact that in the case of μ_0 being normal distribution, all the intermediate densities μ_t are normal as well, i.e, $\mu_t \sim \mathcal{N}(a(t), \Sigma(t))$. Moreover, we can easily obtain ODEs describing how their means and covariances transform (Song et al., 2021b; Särkkä & Solin, 2019). These ODEs take the following form:

$$\frac{d\Sigma(t)}{dt} = 2(I - \Sigma(t)); \quad \frac{da(t)}{dt} = -a(t),$$

with the solutions

$$\Sigma(t) = I + e^{-2t}(\Sigma(0) - I); \quad a(t) = e^{-t}a(0).$$

For the sake of conciseness, let us assume that $a(0) = 0$ (so $a(t) \equiv 0$). We defer the proof of the general case to Appendix A as being slightly more technical. The probability flow ODE then takes the following form:

$$\frac{dx}{dt} = -(I - \Sigma^{-1}(t))x. \quad (15)$$

We start by noticing that all the matrices $\Sigma(t)$ commute with each other. We then can write the solution of Equation (18) as:

$$x(t) = \exp\left(-\int_0^t I - \Sigma^{-1}(\tau)d\tau\right)x(0),$$

with \exp being the matrix exponential. Let us consider the eigendecomposition of $\Sigma(0)$, i.e., assume that $\Sigma(0) = U^T \Lambda U$ with $\Lambda = \text{diag}(\lambda_1, \dots, \lambda_d)$ being a diagonal matrix of positive eigenvalues and $U^T U = I$. We obtain that

$$x(t) = U^T \text{diag}(f(\lambda_1, t), f(\lambda_2, t), \dots, f(\lambda_d, t)) U x(0), \quad (16)$$

where $f(\lambda, t)$ is a function defined as

$$f(\lambda, t) = \exp\left(-\int_0^t 1 - (1 + e^{-2\tau}(\lambda - 1))^{-1} d\tau\right),$$

where now all the functions operate on real numbers. Direct integration shows that:

$$\begin{aligned} f(\lambda, t) &= \exp\left(-t + \frac{1}{2} \log(\lambda - 1 + e^{2t}) - \frac{1}{2} \log \lambda\right) \\ &= \sqrt{\frac{\lambda - 1 + e^{2t}}{\lambda e^{2t}}} = \sqrt{\frac{e^{-2t}(\lambda - 1) + 1}{\lambda}}. \end{aligned} \quad (17)$$

We see that $\lim_{t \rightarrow \infty} f(\lambda, t) = \lambda^{-1/2}$. Then, by definition of the matrix square root, $E_{\mu_0}(x) = \Sigma(0)^{-1/2}x$. This is exactly the optimal transport map between μ_0 and $\mathcal{N}(0, I)$. \square

Discussion. We have shown that for multivariate normal distributions, the probability flow induced by the DDPM diffusion reduces to the optimal transport map in the limit. Note that despite the apparent simplicity of this case, the proof required a non-trivial argument about the probability flow ODE. Moreover, we again note that the trajectories produced by the probability flow ODE are not equal to those of the Benamou-Brenier formulation. Thus, it is hard to attribute this result to a mere coincidence. We hypothesize that the statement of Theorem 3.1 is valid for **arbitrary distributions** (or at least a very large class of distributions), but defer the proof of this statement to future work. For now, we thoroughly evaluate this hypothesis on a large class of synthetic and real distributions.

3.4. Numerical experiments on synthetic data

In this section, we numerically evaluate the aforementioned optimal transport map hypothesis. Setup of our numerical experiments is as follows.

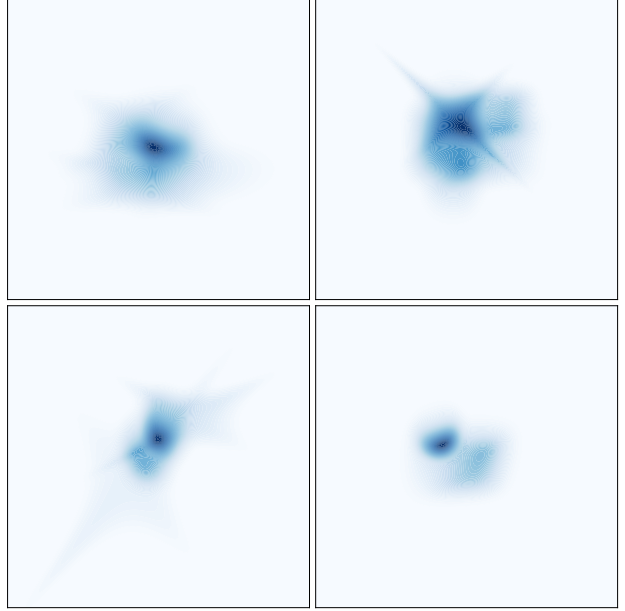


Figure 2: An example of distributions considered for numerical comparison of the Monge optimal transport map against the DDPM encoder map.

Distributions. We consider two-dimensional distributions specified by the following set of parameters: $a_1 \in \mathbb{R}^2$, $a_2 \in \mathbb{R}^2$, $Q_1 \in \mathbb{R}^{2 \times 2}$, $Q_2 \in \mathbb{R}^{2 \times 2}$, with Q_1 and Q_2 being symmetric positive definite. Given these parameters, we set the density $p(x)$ (with $x \in \mathbb{R}^2$) by the following formula.

$$\begin{aligned} p(x) &= \frac{1}{Z} \exp(-q_1(x) - q_2(x)), \\ q_1(x) &= (x - a_1)^T Q_1 (x - a_1), \\ q_2(x) &= ((x - a_2)^2)^T Q_2 (x - a_2)^2, \end{aligned}$$

where the square in q_2 is understood elementwise (so q_2 is a polynomial of degree 4) and Z is a normalizing constant obtained by numerical integration. We then consider uniform mixtures of up to 5 of such randomly generated distributions, i.e.,

$$p(x) = \frac{1}{K} \sum_{i=1}^K p_i(x), \quad K \sim \text{Uniform}(5),$$

with p_i being as above. Some examples are visualized at Figure 2. We see that the distributions are quite diverse and lack any symmetry.

Method. We start by numerically solving the Fokker-Planck equation for an initial density $p(x)$ with the recently proposed approach utilizing low-rank tensor approximations and Chebyshev interpolation (Chertkov & Osledeets, 2021), allowing us to consider sufficiently fine grids. Namely, for spatial dimensions, we utilize 1024 steps for each dimension. As the spatial domain, we consider the square $[-10, 10] \times [-10, 10]$ and densities were scaled beforehand to decay sufficiently fast towards the boundary. For the time dimension, we consider 256 uniform steps in the range $[0, 8]$. For tensor approximations, we utilize the relative accuracy value of 10^{-7} . After obtaining the values of $p_t(x)$, we estimate the score function using finite differences and extend it to the entire spatiotemporal domain via linear interpolation. After these preparations, we sample a set of 2500 points, termed X_0 , from the original density and numerically solve the probability flow ODE (in the time interval $[0, 8]$) with the Runge-Kutta method (DeVries & Wolf, 1994) for each point. The resulting set is denoted as X_1 ; we have $X_1 \sim \mathcal{N}(0, 1)$. Given these two point clouds, X_0 and X_1 , we numerically compute the optimal transport cost with the Python Optimal Transport (POT) library (Flamary et al., 2021). We then compute the transport cost for the map sending a point $x_i \in X_0$ to its counterpart $E_p(x_i) \in X_1$. Our hypothesis suggests that these two costs will be equal up to a reasonable precision.

Experiment and results. We construct 150 random densities and compute two transport costs as described above. We found that in all the experiments those two costs were equal up to relative errors of order 10^{-5} . Here, the relative error is defined as

$$\varepsilon_{rel}(p) = \frac{\text{Cost}(E_p) - \text{Cost}(OT)}{\text{Cost}(OT)}.$$

Scatter plot of the obtained values, as well the histogram of $\log_{10} \varepsilon_{rel}(p)$ is given at Figure 3. We see that up to the numerical precision of our experiment ($\sim 10^{-6}$), these two costs are indeed equal, and in many cases, they were equal up to machine precision. Some examples of the obtained encoder maps are given at Figure 4. We, again, observe that the trajectories of the probability flow ODE are highly nonlinear, despite providing the optimal transport map in the limit.

We conclude that this experiment fully supported our hypothesis. Our code is available at Appendix B.

We now attempt to verify it on a more qualitative level for high-dimensional distributions, where solving the Fokker-Planck equation directly is infeasible. Namely, we consider DDPMs trained on high-resolution image data.

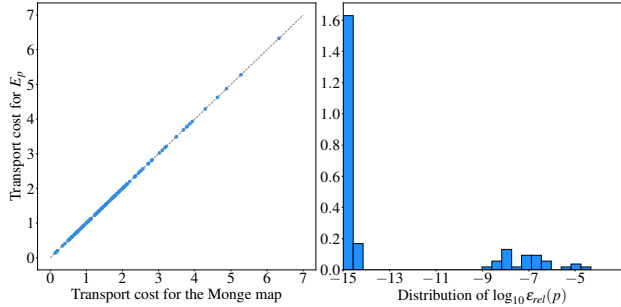


Figure 3: Comparison of transport costs for the optimal Monge map and for the encoder map E_p for a number of sampled densities $p(x)$. We observe that these two values coincide with high precision.

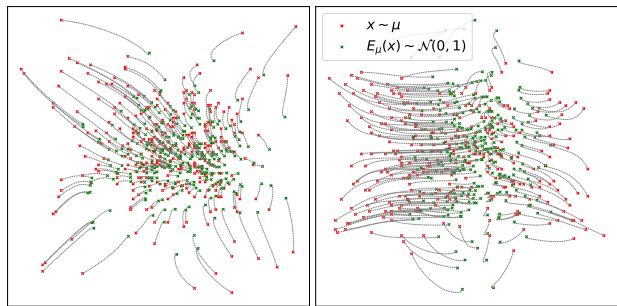


Figure 4: An example of the trajectories of the probability flow ODE and the limiting encoder map for two distributions studied in Section 3.4.

3.5. Experiments of image datasets

Our experiments in this section are organized as follows. Suppose that we are given two datasets and train a DDPM for each dataset. Then, by the hypothesis, each DDPM encoder performs optimal transport from the respective distribution to $\mathcal{N}(0, I)$. Since the optimal transport in our setting is performed in the L_2 sense, for images, this will be reflected by similarity in the pixel space, i.e., high-level texture similarity. We can perform the following experiment to see if this indeed holds. Take a latent code from $\mathcal{N}(0, I)$, and compute a corresponding image from each distribution respectively by reversing the encoder map. We can now compare if these images share texture and a high level semantic structure. Indeed, if each of those images is L_2 -close ‘on average’ to the same latent code, we expect themselves to also be similar on the pixel level. Additionally, on datasets of relatively small sizes, we again can compare the directly computed OT map in the pixel space with the DDPM encoder map.

Datasets. We consider the AFHQ animal dataset (Choi et al., 2020). It consists of 15000 images split into 3 categories: cat, dog, and wild. This is a common benchmark for

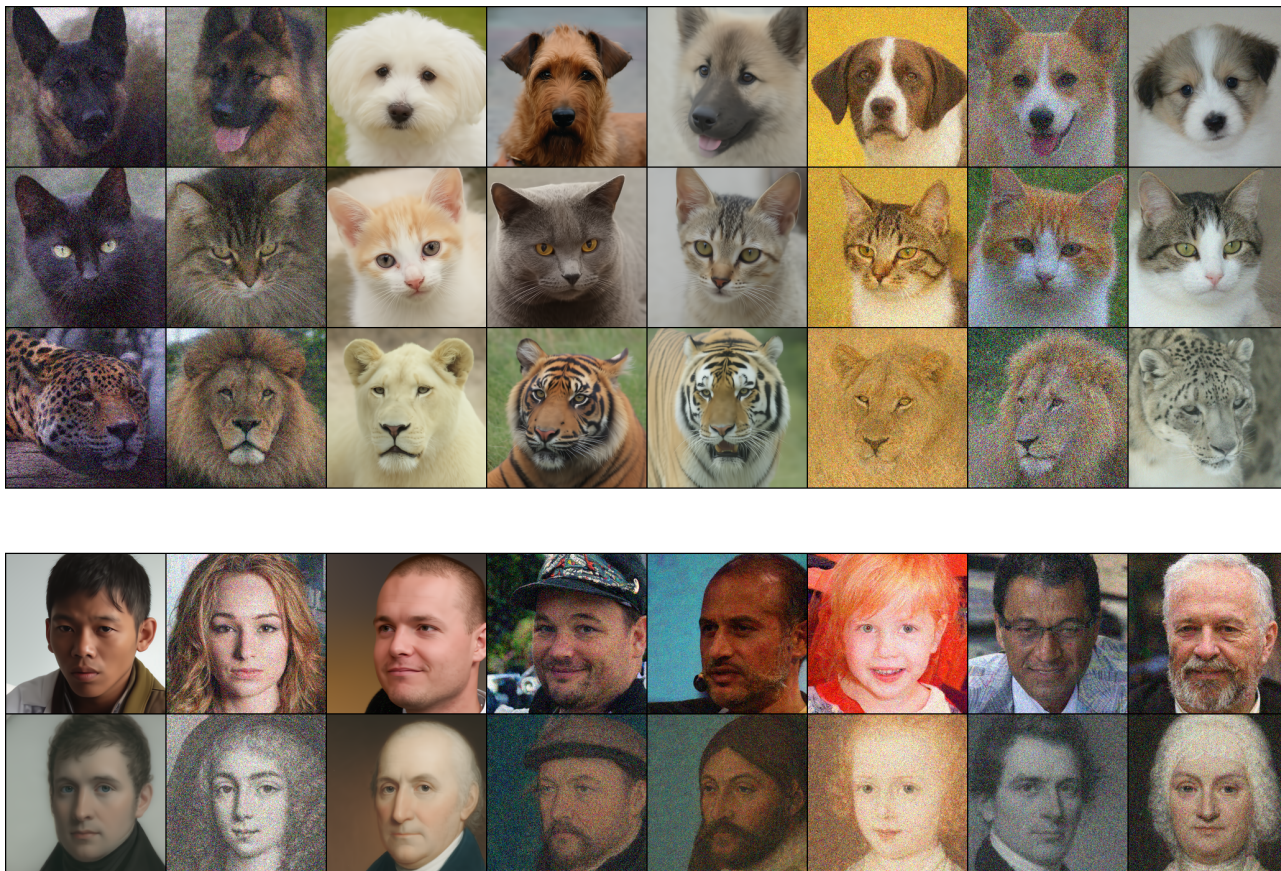


Figure 5: Examples of synthetic samples produced with DDIM sampling from same latent codes. (*Top*) Three independent DDPMs trained on AFHQ *Dog/Cat/Wild*. Each row translates into each row in most cases preserving high-level semantics such as pose and texture, thus supporting the claim of our hypothesis. (*Bottom*) Two DDPMs trained on FFHQ/MetFaces; we note that high-level features such as gender and texture/color are transferred. Interestingly, ‘noisy’ samples seem also to be shared across models.

image-to-image methods. We also verify our theory on the FFHQ dataset of 70,000 human faces (Karras et al., 2019) and the MetFaces dataset (Karras et al., 2020) consisting of 1000 human portraits. Finally, we consider a conditional DDPM on the ImageNet dataset (Deng et al., 2009). By changing the conditioning label, we can control what distribution is being produced, and the argument above still holds.

Models. We consider guided-diffusion, state-of-the-art DDPMs (Dhariwal & Nichol, 2021). We use the official implementation available at [github](https://github.com/openai/guided-diffusion)¹. For each of the datasets we train a separate DDPM model with the same config as utilized for the LSUN datasets in Dhariwal & Nichol (2021) (with dropout); we use default 1000 timesteps for sampling. The AFHQ models were trained for $3 \cdot 10^5$ steps, the FFHQ model was trained for 10^6 steps; for the MetFaces

¹<https://github.com/openai/guided-diffusion>

model, we finetune the FFHQ checkpoint for $25 \cdot 10^3$ steps similar to Choi et al. (2021). All models were trained on 256×256 resolution. For the ImageNet experiment, we utilize the 256 resolution checkpoint for the conditional model available at the GitHub link above.

Algorithm. We follow the aforementioned experimental setup: we sample a number of latent codes from $\mathcal{N}(0, I)$ in the pixel space ($\mathbb{R}^{256 \times 256 \times 3}$) and decode them by different DDPMs with the DDIM algorithm (as was mentioned before, the DDIM algorithm can be viewed as the numerical integration scheme for the probability flow ODE (Salimans & Ho, 2022)). For the ImageNet, we have a single DDPM model but vary the conditioning label.

Qualitative results. We fix a number of latent codes and produce images by all the AFHQ models. The obtained samples are visualized on Figure 5 (top). We observe that samples from different rows indeed share high-level features



Figure 6: Examples of synthetic samples produced with DDIM sampling from same latent codes for different classes with a conditional ImageNet model. We observe that samples share texture and high-level pixel-based similarity.

such as texture and pose. Similarly, we visualize samples from FFHQ and MetFaces on Figure 5 (bottom). We note that samples are aligned in this case as well; notably, in most cases, pose, gender, and various features such as hairstyle and mustache are transferred. Interestingly, artifacts of models such as slight noisiness also seem to be shared.

Results obtained with the ImageNet model are provided at Figure 6. We selected a number of diverse classes, namely, *rooster*, *pizza*, *crab*, *corgi*. We sampled a number of latent codes and produced images by conditioning on the respective label. We see that in this case, high-level textures are transferred as well, sometimes in quite amusing ways (e.g., rooster/pizza rows). As a sanity check, we performed a similar experiment with the conditional BigGAN model (Brock et al., 2019) pretrained on ImageNet. We did not observe similar behavior, suggesting that the texture alignment is an artifact specific to DDPM and not happening simply due to the conditioning mechanism.

Numerical results. We now apply the evaluation scheme of Section 3.4 to the AFHQ dataset. We take the validation subset of each part of the dataset (*Cat/Dog/Wild*) containing 500 images and invert them with DDIM. We then compute the optimal transport matrix between the images and their respective codes (understood as vectors in $\mathbb{R}^{256 \times 256 \times 3}$) with POT. In all three cases, the obtained OT map was the identity matrix, as expected (Figure 7). Given a high dimensionality of the pixel space and a low number of samples, the exact

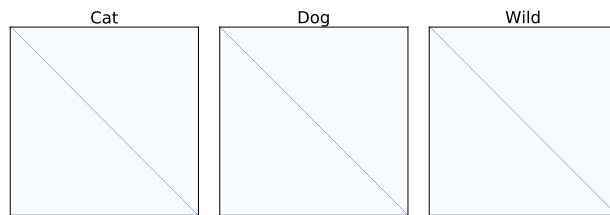


Figure 7: The numerically obtained OT maps between sets of validation images and their respective latent codes on AFHQ. In all three cases, this map is the identity map, confirming our hypothesis.

coincidence with theory is not surprising, as based on Figure 3 for the majority of synthetic experiments, there was an exact match. Intuitively, this should become easier in high dimensions as we may trade some inaccuracies in the model with there being ‘more space’.

To conclude, experiments on real image datasets support our hypothesis and provide interesting examples of how latent codes can be utilized to transfer images from one distribution to another via a ‘proxy’ normal distribution.

4. Related work

In this section, we briefly review the research directions relevant to our study.

Diffusion models (Sohl-Dickstein et al., 2015; Ho et al., 2020) are a class of generative models that approximate the distribution of real images by the endpoint of the Markov chain that originates from a simple parametric distribution, typically a standard Gaussian. Each Markov step is modeled by a deep neural network that effectively learns to invert the diffusion process with a known Gaussian kernel. (Ho et al., 2020) highlighted the equivalence of diffusion models and score matching (Song & Ermon, 2019; 2020), showing them to be two different perspectives on the gradual conversion of a simple known distribution into a target distribution via the iterative denoising process. Very recent works (Nichol & Dhariwal, 2021; Dhariwal & Nichol, 2021) have developed more powerful model architectures as well as different advanced objectives for DDPM, which led to the “victory” of DDPM over GANs in terms of generative quality and diversity. DDPMs have been widely used in applications, including image colorization (Song et al., 2021b), super-resolution (Saharia et al., 2021; Li et al., 2022), inpainting (Song et al., 2021b), semantic editing (Meng et al., 2022), semantic segmentation (Baranchuk et al., 2022).

Optimal transport is a classical area of mathematics tightly related to diffusion processes and PDEs. With hundreds of papers on this topic, we can not provide a thorough review of all the literature and refer the reader to

great texts such as Villani (2009); Ambrosio et al. (2005); Thorpe (2018). While preparing the final version of the manuscript, we discovered that a similar map was utilized to prove certain measure–theoretic inequalities in Kim & Milman (2012). The traditional approach to proving these inequalities used the optimal transport map. Based on this, the authors similarly discuss the question of whether these maps coincide at least when the target distribution is $\mathcal{N}(0, I)$ and were unable to provide a counterexample. They also give a ‘high–level’ proof for the case of multivariate normal distributions, which we prove directly from the ODEs. Rigorous numerical experiments provided in our work confirm that this holds at least for the class of $2d$ -distributions; evidence provided for high–dimensional distributions suggests that this is generally true.

5. Conclusion

In this work, we provided theoretical and experimental evidence that due to the nature of DDPMs, the encoder map turns out to be the optimal transport map. We believe that this result will be interesting to both optimal transport and diffusion models communities. We hope that it will inspire other researchers to obtain general proof of this hypothesis. One observation about the obtained results is that the quadratic cost in the pixel space seems suboptimal when working with visual data. Perhaps, a more elaborate diffusion process leading to feature–based cost may be constructed. We leave this analysis to future work.

References

- Ambrosio, L., Gigli, N., and Savaré, G. *Gradient flows: in metric spaces and in the space of probability measures*. Springer Science & Business Media, 2005. 3, 9
- Baranchuk, D., Voynov, A., Rubachev, I., Khrlukov, V., and Babenko, A. Label-efficient semantic segmentation with diffusion models. In *International Conference on Learning Representations*, 2022. URL <https://openreview.net/forum?id=SlxSY2UZQT>. 8
- Benamou, J.-D. and Brenier, Y. A computational fluid mechanics solution to the Monge-Kantorovich mass transfer problem. *Numerische Mathematik*, 84(3):375–393, 2000. 4
- Brock, A., Donahue, J., and Simonyan, K. Large scale GAN training for high fidelity natural image synthesis. In *International Conference on Learning Representations*, 2019. URL <https://openreview.net/forum?id=B1xsqj09Fm>. 8
- Chertkov, A. and Oseledets, I. Solution of the Fokker–Planck Equation by Cross Approximation Method in the Tensor Train Format. *Frontiers in Artificial Intelligence*, 4, 2021. doi: 10.3389/frai.2021.668215. URL <https://www.frontiersin.org/article/10.3389/frai.2021.668215>. 6
- Choi, J., Kim, S., Jeong, Y., Gwon, Y., and Yoon, S. ILVR: Conditioning method for denoising diffusion probabilistic models. *Proceedings of the IEEE international conference on computer vision*, 2021. 7
- Choi, Y., Uh, Y., Yoo, J., and Ha, J.-W. Stargan v2: Diverse image synthesis for multiple domains. In *Proceedings of the IEEE/CVF Conference on Computer Vision and Pattern Recognition*, pp. 8188–8197, 2020. 6
- Deng, J., Dong, W., Socher, R., Li, L.-J., Li, K., and Fei-Fei, L. Imagenet: A large-scale hierarchical image database. In *2009 IEEE conference on computer vision and pattern recognition*, pp. 248–255. Ieee, 2009. 7
- DeVries, P. L. and Wolf, R. P. A first course in computational physics. *Computers in Physics*, 8(2):178–179, 1994. 6
- Dhariwal, P. and Nichol, A. Q. Diffusion models beat GANs on image synthesis. In Beygelzimer, A., Dauphin, Y., Liang, P., and Vaughan, J. W. (eds.), *Advances in Neural Information Processing Systems*, 2021. URL <https://openreview.net/forum?id=AAWuCVzaVt>. 1, 7, 8
- Flamary, R., Courty, N., Gramfort, A., Alaya, M. Z., Boisbunon, A., Chambon, S., Chapel, L., Corenflos, A., Fatras, K., Fournier, N., Gautheron, L., Gayraud, N. T., Janati, H., Rakotomamonjy, A., Redko, I., Rolet, A., Schutz, A., Seguy, V., Sutherland, D. J., Tavenard, R., Tong, A., and Vayer, T. POT: Python Optimal Transport. *Journal of Machine Learning Research*, 22(78):1–8, 2021. URL <http://jmlr.org/papers/v22/20-451.html>. 6
- Givens, C. R. and Shortt, R. M. A class of Wasserstein metrics for probability distributions. *Michigan Mathematical Journal*, 31(2):231–240, 1984. 4
- Gorham, J. *Measuring sample quality with Stein’s method*. Stanford University, 2017. 2

- Ho, J., Jain, A., and Abbeel, P. Denoising Diffusion Probabilistic Models. In Larochelle, H., Ranzato, M., Hadsell, R., Balcan, M. F., and Lin, H. (eds.), *Advances in Neural Information Processing Systems*, volume 33, pp. 6840–6851. Curran Associates, Inc., 2020. URL <https://proceedings.neurips.cc/paper/2020/file/4c5bcfec8584af0d967f1ab10179ca4b-Paper.pdf>. 1, 8
- Karras, T., Laine, S., and Aila, T. A style-based generator architecture for generative adversarial networks. In *Proceedings of the IEEE/CVF Conference on Computer Vision and Pattern Recognition*, pp. 4401–4410, 2019. 7
- Karras, T., Aittala, M., Hellsten, J., Laine, S., Lehtinen, J., and Aila, T. Training generative adversarial networks with limited data. In *Proc. NeurIPS*, 2020. 7
- Kim, Y.-H. and Milman, E. A generalization of Caffarelli’s contraction theorem via (reverse) heat flow. *Mathematische Annalen*, 354(3):827–862, 2012. 9
- Li, H., Yang, Y., Chang, M., Chen, S., Feng, H., Xu, Z., Li, Q., and Chen, Y. SRDiff: Single Image Super-resolution with Diffusion Probabilistic Models. *Neurocomputing*, 2022. ISSN 0925-2312. doi: <https://doi.org/10.1016/j.neucom.2022.01.029>. URL <https://www.sciencedirect.com/science/article/pii/S0925231222000522>. 1, 8
- Liu, Q., Lee, J., and Jordan, M. A kernelized Stein discrepancy for goodness-of-fit tests. In *International conference on machine learning*, pp. 276–284. PMLR, 2016. 2
- Meng, C., He, Y., Song, Y., Song, J., Wu, J., Zhu, J.-Y., and Ermon, S. SDEdit: Guided image synthesis and editing with stochastic differential equations. In *International Conference on Learning Representations*, 2022. URL https://openreview.net/forum?id=aBsCjcPu_tE. 1, 2, 8
- Nichol, A. and Dhariwal, P. Improved denoising diffusion probabilistic models. *ICML*, 2021. 2, 8
- Otto, F. *Double degenerate diffusion equations as steepest descent*. Citeseer, 1996. 3
- Otto, F. The geometry of dissipative evolution equations: the porous medium equation. 2001. 3
- Risken, H. Fokker-Planck equation. In *The Fokker-Planck Equation*, pp. 63–95. Springer, 1996. 2
- Saharia, C., Ho, J., Chan, W., Salimans, T., Fleet, D. J., and Norouzi, M. Image super-resolution via iterative refinement. 2021. 1, 8
- Salimans, T. and Ho, J. Progressive distillation for fast sampling of diffusion models. In *International Conference on Learning Representations*, 2022. URL <https://openreview.net/forum?id=TIIdIXIpzhoI>. 2, 7
- Särkkä, S. and Solin, A. *Applied stochastic differential equations*, volume 10. Cambridge University Press, 2019. 3, 4
- Sohl-Dickstein, J., Weiss, E., Maheswaranathan, N., and Ganguli, S. Deep unsupervised learning using nonequilibrium thermodynamics. In *International Conference on Machine Learning*, pp. 2256–2265. PMLR, 2015. 1, 8
- Song, J., Meng, C., and Ermon, S. Denoising Diffusion Implicit Models. In *International Conference on Learning Representations*, 2021a. URL <https://openreview.net/forum?id=StlgIarCHLP>. 1, 2
- Song, Y. and Ermon, S. Generative modeling by estimating gradients of the data distribution. In Wallach, H., Larochelle, H., Beygelzimer, A., d’Alché-Buc, F., Fox, E., and Garnett, R. (eds.), *Advances in Neural Information Processing Systems*, volume 32. Curran Associates, Inc., 2019. URL <https://proceedings.neurips.cc/paper/2019/file/3001ef257407d5a371a96dcd947c7d93-Paper.pdf>. 8
- Song, Y. and Ermon, S. Improved techniques for training score-based generative models. In Larochelle, H., Ranzato, M., Hadsell, R., Balcan, M. F., and Lin, H. (eds.), *Advances in Neural Information Processing Systems*, volume 33, pp. 12438–12448. Curran Associates, Inc., 2020. URL <https://proceedings.neurips.cc/paper/2020/file/92c3b916311a5517d9290576e3ea37ad-Paper.pdf>. 8
- Song, Y., Sohl-Dickstein, J., Kingma, D. P., Kumar, A., Ermon, S., and Poole, B. Score-based generative modeling through stochastic differential equations. In *International Conference on Learning Representations*, 2021b. URL <https://openreview.net/forum?id=PxTIG12RRHS>. 1, 2, 3, 4, 8
- Stein, C. A bound for the error in the normal approximation to the distribution of a sum of dependent random variables. In *Proceedings of the sixth Berkeley symposium on mathematical statistics and probability, volume 2: Probability theory*, volume 6, pp. 583–603. University of California Press, 1972. 2
- Thorpe, M. Introduction to optimal transport, 2018. 3, 9
- Villani, C. Optimal transportation, dissipative pde’s and functional inequalities. In *Optimal transportation and applications*, pp. 53–89. Springer, 2003. 4
- Villani, C. *Optimal transport: old and new*, volume 338. Springer, 2009. 3, 4, 9

A. Proof of Theorem 3.1

Here we provide a complete proof of Theorem 3.1

Theorem 3.1. *Let $\mu_0 \sim \mathcal{N}(a(0), \Sigma(0))$ be a multivariate normal distribution. Then E_{μ_0} is the Monge optimal transport map between μ_0 and $\mathcal{N}(0, I)$, i.e.,*

$$E_{\mu_0}(x) = \Sigma(0)^{-1/2}(x - a(0)).$$

Proof. Proof for the case $a(0) = 0$ was given in the main text. For a general case, we obtain the following ODE.

$$\frac{dx}{dt} = -(I - \Sigma^{-1}(t))x - \Sigma^{-1}(t)a(t). \quad (18)$$

This is an inhomogeneous ODE. We can obtain its solution via the following standard approach. Let $Z(t)$ be the fundamental solution of the homogeneous part, found in the main text (16). I.e.,

$$Z(t) = U^T \text{diag}(f(\lambda_1, t), f(\lambda_2, t), \dots, f(\lambda_d, t))U,$$

with

$$f(\lambda, t) = \sqrt{\frac{e^{-2t}(\lambda - 1) + 1}{\lambda}}.$$

We find that a particular solution (with 0 initial condition) of the inhomogeneous problem is given by:

$$\bar{x}(t) = -Z(t) \int_0^t Z^{-1}(\tau) \Sigma^{-1}(\tau) a(\tau) d\tau.$$

Recall that

$$\Sigma(t) = I + e^{-2t}(\Sigma(0) - I); \quad a(t) = e^{-t}a(0).$$

We obtain:

$$\bar{x}(t) = \left(-Z(t) \int_0^t Z^{-1}(\tau) \Sigma^{-1}(\tau) e^{-\tau} d\tau \right) a(0).$$

Again, it suffices to work on the level of the spectrum. I.e.,

$$\bar{x}(t) = U^T \text{diag}(g(\lambda_1, t), g(\lambda_2, t), \dots, g(\lambda_d, t))U a(0),$$

with

$$\begin{aligned} g(\lambda, t) &= -f(\lambda, t) \int_0^t \frac{e^{-\tau}}{(1 + e^{-2\tau}(\lambda - 1))f(\lambda, \tau)} d\tau \\ &= -\frac{f(\lambda, t)}{\lambda} \int_0^t \frac{e^{-\tau}}{f^3(\lambda, \tau)} d\tau \\ &= -\sqrt{\lambda} f(\lambda, t) \int_0^t \frac{e^{-\tau}}{(e^{-2\tau}(\lambda - 1) + 1)^{3/2}} d\tau. \end{aligned} \quad (19)$$

Direct integration shows that:

$$\lim_{t \rightarrow \infty} g(\lambda, t) = -\frac{1}{\sqrt{\lambda}}.$$

Thus, we obtain that

$$\lim_{t \rightarrow \infty} \bar{x}(t) = -\Sigma(0)^{-1/2}a(0).$$

By combining this piece with the limit of general solution obtained in the main text, we find that

$$E_{\mu_0}(x) = \Sigma(0)^{-1/2}x - \Sigma(0)^{-1/2}a(0) = \Sigma^{-1/2}(0)(x - a(0)),$$

which is exactly the desired optimal transport map in the general case. \square

B. Code

Our code is available at this [dropbox link](#).